PHYSICAL REVIEW B **112**, 085422 (2025)

Editors' Suggestion

Initialization of neutral and charged exciton spin states in a telecom-emitting quantum dot

Giora Peniakov,[1,*,†] Johannes M. Michl,[1,*] Mohamed Helal,[1] Raphael Joos,[2] Michael Jetter,[2]
Simone L. Portalupi,[2] Peter Michler,[2] Sven Höfling,[1] and Tobias Huber-Loyola[1]
[1]*Julius-Maximilians-Universität Würzburg, Physikalisches Institut, Lehrstuhl für Technische Physik, Am Hubland, 97074 Würzburg, Germany*
[2]*Institut für Halbleiteroptik und Funktionelle Grenzflächen (IHFG), Center for Integrated Quantum Science and Technology (IQST) and SCoPE, University of Stuttgart, Allmandring 3, 70569 Stuttgart, Germany*

(Received 6 May 2025; accepted 8 July 2025; published 25 August 2025)

Photonic cluster states are highly entangled states that allow for photonic quantum computing and memoryless quantum repeaters. Their generation has been recently demonstrated using semiconductor quantum dots emitting at the 900 nm wavelength range. However, a similar demonstration at the communication-optimal telecom range has remained elusive. A key ingredient that is still missing is an appropriate optical excitation method. A central requirement of such a method is to allow an arbitrary spin initialization of quantum-dot excitonic complexes. In this work, we report on developing such a method based on a quasiresonant p-shell excitation for an InAs/InGaAs quantum dot emitting at 1535 nm. We show qubit writing of a neutral exciton and spin-preserving excitation of a negative trion. Using the Larmor precession of the negative trion under an externally applied magnetic field, we determine the in-plane g factors of both the electron and the hole in the investigated quantum dot. In addition, we measure a lower bound on the hole coherence time, $T_2^* > 6.4\,\mathrm{ns}$, boosting its candidacy as a sound photon entangler for more advanced quantum photonic schemes.

DOI: 10.1103/3qh7-b696

I. INTRODUCTION

Quantum computing and quantum communication have captured the imagination of many who seek to exploit quantum phenomena in everyday life. For quantum computing, several technological platforms are being studied: superconducting qubits, trapped ions and atoms, photonic qubits, and others [1–4]. Photonic qubits have the advantage of low interaction with the environment, but for the use in quantum computing their wavelength has to be compatible with the processor unit [5,6]. For quantum communication, on the other hand, only photonic qubits are suitable [7]. They can be transmitted long distances while carrying quantum information encoded in their polarization [8] or in the time domain [9]. Since most of the communication is based on fused-silica optical fibers, the wavelength of the photons should be chosen to minimize their losses. The telecom C-band, spanning between 1530 and 1560 nm, has proven to have minimal absorption in fused silica and therefore is the optimal choice.

Protocols that exploit photons for quantum communication suggest generating the photons in highly entangled graph states [10–12]. These so-called cluster states are also the fundamental resource for photonic quantum computing. A proven way to create linear cluster states, which can be fused to larger, more complex units [13], is by using semiconductor quantum dots (QDs) as photon sources. In 2016, Schwartz *et al.* showed a first demonstration of how a photonic cluster state can be generated by repetitive excitation of a QD-confined matter spin [14]. While in this demonstration the matter spin that was used was a dark exciton, it was later shown that a heavy hole is an even better choice, producing photons that are also indistinguishable [15]. These and other works [16–19] were based on QDs emitting at the near-infrared wavelength range around 900 nm or on neutral ^{87}Rb atoms below 800 nm emission wavelength [20]. At the optimal range for communication, i.e., the telecom C-band, such a demonstration is still posing a challenge.

Much progress has been made in recent years developing QD photonic sources that emit at the telecom C-band range. These sources have been proven to be bright and produce single indistinguishable photons [21,22] with low multiphoton contributions. More advanced benchmarks have been achieved as well, including full spin control [23], spin-photon entanglement [24], and the generation of polarization-entangled pairs [25,26]. However, for generating a photonic cluster state, a key ingredient has remained elusive—spin state initialization using a nonresonant excitation. While spin initialization using resonant excitation has already been demonstrated [23,24], this method suffers from the drawback of requiring a polarization-rejection optical setup. Since the protocol for generating cluster states utilizes polarization as the degree of freedom for qubit encoding, its realization in cross-polarization setups renders it impossible [10].

In this work, we demonstrate spin state initialization using a p-shell quasiresonant excitation on two different excitonic

---

[*] These authors contributed equally to this work.

[†] Contact author: giora.peniakov@uni-wuerzburg.de

complexes: the neutral exciton X^0 and the negatively charged trion X^-. In the first case, we initialize the X^0 in an arbitrary spin state using the polarization of a quasiresonant laser pulse. We show a one-to-one correspondence between the laser polarization and the spin orientation, known in the literature as qubit writing [27,28]. In a second QD, we show polarization memory of the X^- optical transition: Exciting a confined electron with circularly polarized light leads to an emission with the same polarization. Moreover, applying an in-plane magnetic field, we observe the Larmor precessions of both the X^- and the ground-state electrons. These measurements also allow us to extract the in-plane electron and hole g factors in the studied QDs, and to set a lower bound on the hole coherence time T_2^*.

We start this paper by mathematically describing the X^0 and X^- two-level systems, including their selection rules for optical transitions. This description is useful since much of the results in this work are based on spin-precession observation. Experimentally, we detect those precessions in the photoluminescence (PL) by observing oscillations in its degree of polarization (DOP). Understanding these oscillations is therefore key in deriving the conclusions of this work.

The selection rules of excitonic two-level systems

In this section, we compare the spin dynamics of the X^0 and X^-, and show that they lead to a different polarization signal.

1. Neutral exciton, X^0

We start by defining the photon polarization basis as follows:

$$\text{R/L Basis}\qquad \begin{aligned} &\sqrt{2}\,|H\rangle = |R\rangle + |L\rangle\,, && -\sqrt{2}i\,|V\rangle = |R\rangle - |L\rangle\,,\\ &\sqrt{2}\,|D\rangle = e^{-i\pi/4}(|R\rangle + i\,|L\rangle), && \sqrt{2}\,|A\rangle = e^{+i\pi/4}(|R\rangle - i\,|L\rangle), \end{aligned} \tag{1}$$

where $|H\rangle$, $|V\rangle$, $|D\rangle$, $|A\rangle$, $|R\rangle$, and $|L\rangle$ denote the horizontal, vertical, diagonal, antidiagonal, right-hand circular, and left-hand circular polarization, respectively. The R/L basis lies along the symmetry axis of the QD, $\hat{z}$, which is also the optical path direction perpendicular to the sample. In the Pauli matrices notation, the polarization R/L basis coincides with the computational basis $|\pm Z\rangle$. The extra i phase suggested in the $|V\rangle$ definition ensures that the relations between circular and rectilinear polarizations follow the standard polarization convention for constructing $|R\rangle$ and $|L\rangle$ from a superposition of $|H\rangle$ and $|V\rangle$. Below, we list the complete set of polarization relations in the H/V basis, useful for the following calculations:

$$\text{H/V Basis}\qquad \begin{aligned} &\sqrt{2}\,|R\rangle = |H\rangle - i\,|V\rangle\,, && \sqrt{2}\,|L\rangle = |H\rangle + i\,|V\rangle\,,\\ &\sqrt{2}\,|D\rangle = |H\rangle - |V\rangle\,, && \sqrt{2}\,|A\rangle = |H\rangle + |V\rangle\,. \end{aligned} \tag{2}$$

In parallel, we can describe the X^0 two-level system using the Pauli matrices eigenstates $|+X\rangle$, $|-X\rangle$, $|+Y\rangle$, $|-Y\rangle$, $|+Z\rangle$, and $|-Z\rangle$, and set a one-to-one correspondence between them and the polarization states,

$$\begin{aligned} &|H\rangle \leftrightarrow |+X\rangle\,, && |D\rangle \leftrightarrow |+Y\rangle\,, && |R\rangle \leftrightarrow |+Z\rangle\,,\\ &|V\rangle \leftrightarrow |-X\rangle\,, && |A\rangle \leftrightarrow |-Y\rangle\,, && |L\rangle \leftrightarrow |-Z\rangle\,. \end{aligned} \tag{3}$$

This correspondence ensures that the X^0 states follow the same relations defined for the polarizations in Eqs. (1) and (2). In the typical case where the QD shape deviates from a perfect cylindrical symmetry, the degeneracy of the X^0 two-level system is lifted, creating a fine-structure splitting (FSS), with an energy difference E_{FSS}. We set the direction of this asymmetry as $\hat{x}$, making the $|\pm X\rangle$ states eigenstates and, consequently, redefining the reference frame for the H and V polarizations. Under these definitions, an arbitrary initial X^0 state $|\psi(t=0)\rangle = \alpha\,|+X\rangle + \beta\,|-X\rangle$ (with α and β complex numbers, and $|\alpha|^2 + |\beta|^2 = 1$) evolves in time according to the Schrödinger equation:

$$\text{Time evolution}\qquad |\psi(t)\rangle = \alpha e^{\frac{-iE_{\text{FSS}}t}{2\hbar}}\,|+X\rangle + \beta e^{\frac{+iE_{\text{FSS}}t}{2\hbar}}\,|-X\rangle\,. \tag{4}$$

Geometrically, this evolution can be described as a rotation in the Bloch sphere around the eigenstate axis connecting the antipodal points $|+X\rangle$ and $|-X\rangle$ [see Fig. 1(a)]. Since the X^0 is an electron-hole pair, it couples to an empty QD solely by absorbing or emitting a single photon. In general, the selection rules for optical transitions in the QD are along its symmetry axis, which we label $\hat{z}$. However, the X^0 single-photon coupling to the vacuum means that there is a one-to-one correspondence between the X^0 state and the photon polarization: a state $|\psi\rangle = \alpha\,|+X\rangle + \beta\,|-X\rangle$ couples to a photon with polarization $|P\rangle = \alpha\,|H\rangle + \beta\,|V\rangle$. Consequently, the natural precession of the X^0 (induced by its FSS) can be observed in the polarization of the photon it emits upon optical recombination. As an example, we consider the X^0 prepared in the initial state $\sqrt{2}\,|\psi_0\rangle = |+X\rangle + |-X\rangle$ (equal to the state $\sqrt{2}\,|-Y\rangle$) which then evolves according to Eq. (4). Its projection probabilities on the three Bloch sphere directions as a function of time are

$$\begin{aligned} |\langle \pm X|\psi(t)\rangle|^2 &= \tfrac{1}{2},\\ |\langle \pm Y|\psi(t)\rangle|^2 &= \tfrac{1}{2}(1 \mp \cos 2\omega t),\\ |\langle \pm Z|\psi(t)\rangle|^2 &= \tfrac{1}{2}(1 \mp \sin 2\omega t), \end{aligned} \tag{5}$$

where we define the frequency as $\omega = E_{\text{FSS}}/2\hbar$. These projection probabilities explicitly represent the polarization of the

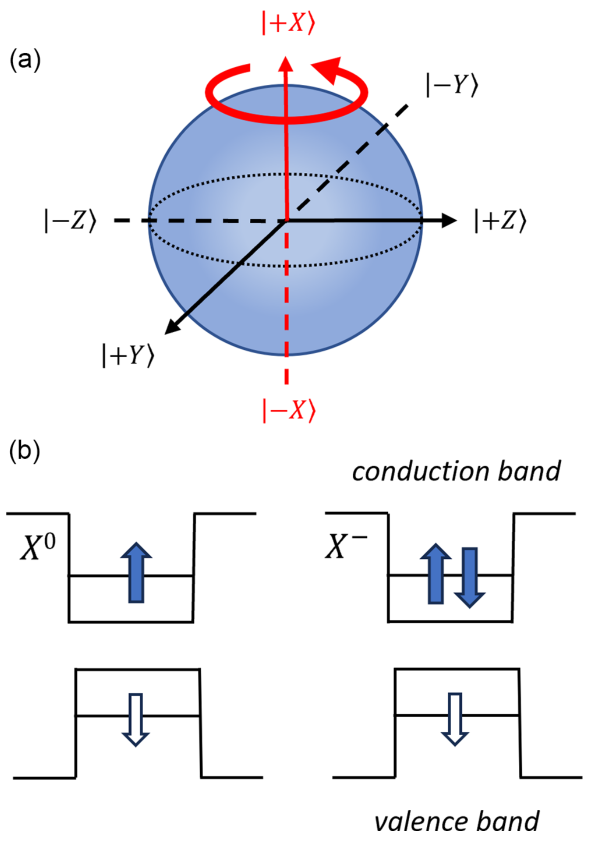

FIG. 1. X^0 and X^-. (a) Bloch sphere of the X^0 spin two-level system. (b) Occupation sketches of the X^0 and X^-. Without loss of generality, the hole spin direction is chosen to be down.

emitted light in the experiment,

$$\langle H/V\rangle = |\langle \pm X|\psi(t)\rangle|^2, \quad \langle D/A\rangle = |\langle \pm Y|\psi(t)\rangle|^2,$$
$$\langle R/L\rangle = |\langle \pm Z|\psi(t)\rangle|^2. \tag{6}$$

Then, the measured degree of polarization (DOP) in each basis is defined by

$$\mathrm{DOP}_X = \frac{\langle H\rangle - \langle V\rangle}{\langle H\rangle + \langle V\rangle}, \quad \mathrm{DOP}_Y = \frac{\langle D\rangle - \langle A\rangle}{\langle D\rangle + \langle A\rangle},$$
$$\mathrm{DOP}_Z = \frac{\langle R\rangle - \langle L\rangle}{\langle R\rangle + \langle L\rangle}. \tag{7}$$

Plugging the projection probabilities of Eq. (5) into the DOPs yields

$$\mathrm{DOP}_X = 0, \quad \mathrm{DOP}_Y = -\cos\frac{E_{\mathrm{FSS}}t}{\hbar},$$
$$\mathrm{DOP}_Z = -\sin\frac{E_{\mathrm{FSS}}t}{\hbar}. \tag{8}$$

2. Charged exciton, $X^{\pm}$

The case of the trion, $X^{\pm}$, is slightly different. It comprises three charge carriers, where an electron-hole pair recombination renders the QD with a single charge. The spin of this charge is often called the ground-level spin, while the spin of the trion itself, governed by the unpaired charge carrier, is called the excited-level spin [29]. For example, in the case of the negative trion X^-, the ground-level spin is an electron while the excited-level spin is the X^- itself. However, since both of the X^- electrons reside in their lowest s-shell energy level, they form a singlet and therefore do not contribute to the overall angular momentum. The unpaired hole, then, governs the spin of the entire excited level.

First, we assume the $X^{\pm}$ is prepared in the state $\sqrt{2}\,|\psi_0^T\rangle = |T_+\rangle + |T_-\rangle$, similarly to our previous discussion on the X^0. In this notation, $|T_{\pm}\rangle$ are the equivalent states to the neutral exciton's $|\pm X\rangle$. They follow the states' relations specified in Eqs. (1) and (2). For example, $\sqrt{2}\,|T_+\rangle = |T_{\uparrow}\rangle + |T_{\downarrow}\rangle$, where the states $|T_{\uparrow/\downarrow}\rangle$ correspond to the computation basis and are equivalent to the X^0's $|\pm Z\rangle$. We further assume that applying an external magnetic field splits the $|T_{\pm}\rangle$ states by an amount δ, playing a similar role as the excitonic FSS. As a function of time, the state $|\psi_0^T\rangle$ evolves into

$$\sqrt{2}\,|\psi^T(t)\rangle = e^{-i\omega t}\,|T_+\rangle + e^{+i\omega t}\,|T_-\rangle\,, \tag{9}$$

where $\omega = \delta/2\hbar$. As before, the selection rules for optical transition are along the $\hat{z}$ direction and read $|T_{\uparrow}\rangle \mapsto |\uparrow\rangle\,|R\rangle$ and $|T_{\downarrow}\rangle \mapsto |\downarrow\rangle\,|L\rangle$, where $|\uparrow / \downarrow\rangle$ are the single charge-carrier spin projections parallel to $|T_{\uparrow/\downarrow}\rangle$. Upon electron-hole recombination, the spin of the rendered charge carrier and the emitted photon polarization form the joint superposition,

$$|\psi(t)\rangle = \tfrac{1}{2}[(e^{-i\omega t} + ie^{+i\omega t})\,|\uparrow\rangle\,|R\rangle + (e^{-i\omega t} - ie^{+i\omega t})\,|\downarrow\rangle\,|L\rangle\,. \tag{10}$$

Calculating the projections $|\langle H, V, D, A, R, L|\psi(t)\rangle|^2$ and then the resulting DOPs, we obtain

$$\mathrm{DOP}_X = 0, \quad \mathrm{DOP}_Y = 0, \quad \mathrm{DOP}_Z = -\sin\frac{\delta t}{\hbar}. \tag{11}$$

Note that assuming a different selection rule, say, $|T_{\pm Y}\rangle \mapsto |D/A\rangle\,|\pm Y\rangle$, would produce a different result from Eq. (11).

Comparing Eqs. (8) and (11), one sees a substantial difference between the X^- and the X^0 case: while for the X^0, oscillations in the emitted polarization are expected both in the Z and Y bases, for the $X^{\pm}$, they are expected only in Z. The main difference between the two cases stems from the difference in the final states of these two optical transitions: while the X^0 decays into vacuum, the X^- decays into another two-level system, i.e., the electron.

In the next section, we will examine this difference experimentally. We will show that we can write an arbitrary superposition onto the X^0 state and prove it, while on the X^- we can only initialize in two spin states, $|T_{\uparrow/\downarrow}\rangle$.

II. RESULTS

We present a spectroscopic study of two InAs/InGaAs QDs.

A. Neutral exciton, X^0

1. Time-independent spectroscopy

Figure 2(a) shows a polarization-resolved micro-photoluminescence (μ-PL) spectrum of a selected QD1. Several spectral lines of discrete optical transitions portray a typical QD emission at 1530–1540 nm. For excitation, we use a 1064 nm above-band-gap continuous-wave (CW) laser.

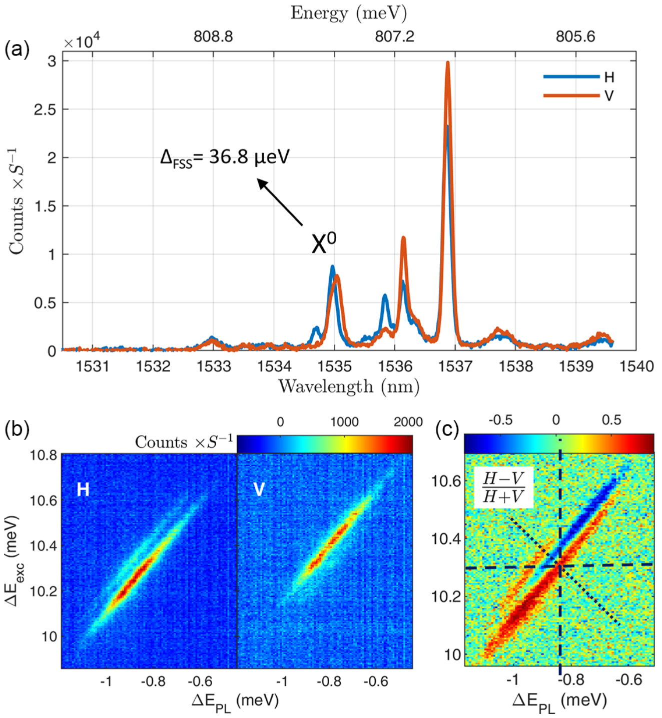

FIG. 2. X^0 PL and PLE. (a) PL spectrum of QD1 projected on H and V polarizations. (b) PLE of the X^0, concentrated on its p-shell quasiresonance found around 10 meV above the X^0 emission. The quasiresonance is shown under two polarization conditions: in the left pane, both excitation and detection are H; in the right pane, both are V. (c) DOP of (b). Values close to 1 (-1) are marked red (blue) corresponding to H (V) polarization. Dashed lines are guides to the eye showing different directions of the calculated energy splitting (see text).

We identify the high-energy line at ~1535 nm as the neutral exciton, X^0. This identification is based on (i) observation of a polarized FSS of 36.8 ± 2.6 µeV, (ii) its high-energy spectral position, compatible with the characteristic low binding energy of an X^0 relative to other excitonic complexes, and (iii) occupation statistics under a power series measurement: an increase in the excitation power reveals the X^0 line as among the first to appear, indicating its low-number-of-particles structure. Based on the FSS measured polarization, we redefine the H and V polarization directions of our setup to match the orientation of the QD.

To identify the quasiresonances of the QD, we perform a photoluminescence excitation (PLE) scan. For that, we use a CW excitation laser with a tunable wavelength between ~1460 and 1527 nm. In energy terms, this range covers about 37 meV: from 4.2 to 41.5 meV above the X^0 emission. Figure 2(b) shows a part of this scan where we detect a quasiresonance at approximately 10.3 meV. Similarly to the μ-PL in Fig. 2(a), we measure this PLE in two polarization conditions: one where both the excitation and the detection are set to H, and one where both are set to V. We make several observations:

(1) The X^0 emission energy in the PLE is shifted compared to its emission under above-band-gap excitation (where $\Delta E_{\mathrm{PL}} = 0$). This shift, relative to the central wavelength of the quasiresonance, is approximately $\Delta E_{\mathrm{PL}} = -0.8$ meV. A possible explanation for that is the Stark effect caused by charge accumulation in the vicinity of the QD: we conjecture that changing the excitation wavelength from above band gap to below band gap (which the PLE scanning laser is) changes the charge environment of the QD. As a result, different electric fields are induced in the QD, modifying confined energy levels and spectrally shifting the PL. Excitation power, on the other hand, only weakly affects the spectral position of the lines (not shown). This observation is reminiscent of the photoelectric effect and strengthens our conjecture about wavelength-dependent varying charge environment.

(2) The quasiresonance has a diagonal-shape profile with width and height (along ΔE_{PL} and ΔE_{exc}) of roughly 0.5 and 0.6 meV, respectively. Its slope is, therefore, 1.22 ± 0.02. Note that the spectral width of 0.5 meV is an order of magnitude larger than the resolved linewidth of the spectral line, which we measure around 80 µeV. As of the time of writing, the origin of the quasiresonance diagonal shape remains unclear for us.

(3) The quasiresonance also reveals an FSS of the p shell. As a function of the laser energy only, ΔE_{exc}, this splitting is 49 ± 4 µeV [vertical direction in Fig. 2(c)]. Perpendicular to the diagonal, it is 31 ± 4 µeV (fine-dashed line). Examples of similar values for p-shell FSS can be found in Ref. [30].

2. *Polarization-resolved time-dependent spectroscopy*

To demonstrate qubit writing on the X^0, we measure its time-dependent emission after pulsed laser excitation. The laser pulse duration is around 15 ps, and its wavelength 1514.4 nm, matching the X^0 quasiresonance presented earlier in Fig. 2(b). The emission is recorded using superconducting nanowire single-photon detectors (SNSPDs) with a response time jitter of around 28 ps. To control the polarization of the excitation and detection channels, we use liquid-crystal variable retarders (LCVRs). By periodically changing the polarization of each channel between H, V, D, A, R, and L, we recorded $6\times6 = 36$ time traces of different excitation-detection combinations. In Fig. 3, we present only six of them, best illustrating the X^0 selection rules for optical recombination (the full set of 36 appears in the Supplemental Material [31]). Since here we are mostly interested in the oscillation dynamics, we normalized each time trace by the time-integrated signal (i.e., by the area beneath each decay). We often refer to this measurement as a "polarization-resolved lifetime measurement." The lifetime here was measured to $\tau = 1015 \pm 10$ ps.

In Figs. 3(a)–3(c), we excite the X^0 using R-,D-, and H-polarized pulses and project the signal on the corresponding bases, R/L, D/A, and H/V. In the R/L and D/A bases, clear oscillations of the X^0 are observed. A phase shift of π is evident between the oscillations in the co- and cross polarizations (blue and red curves). The lower panels of Figs. 3(a)–3(c) show the DOP of the oscillations, from which we extract the oscillation period, $T = 114 \pm 1.5$ ps. This value corresponds to an energy splitting of $\Delta E = 2\pi\hbar/T = 36.17 \pm 0.47$ µeV, in good agreement with the spectrally measured FSS mentioned earlier, 36.8 ± 2.6 µeV.

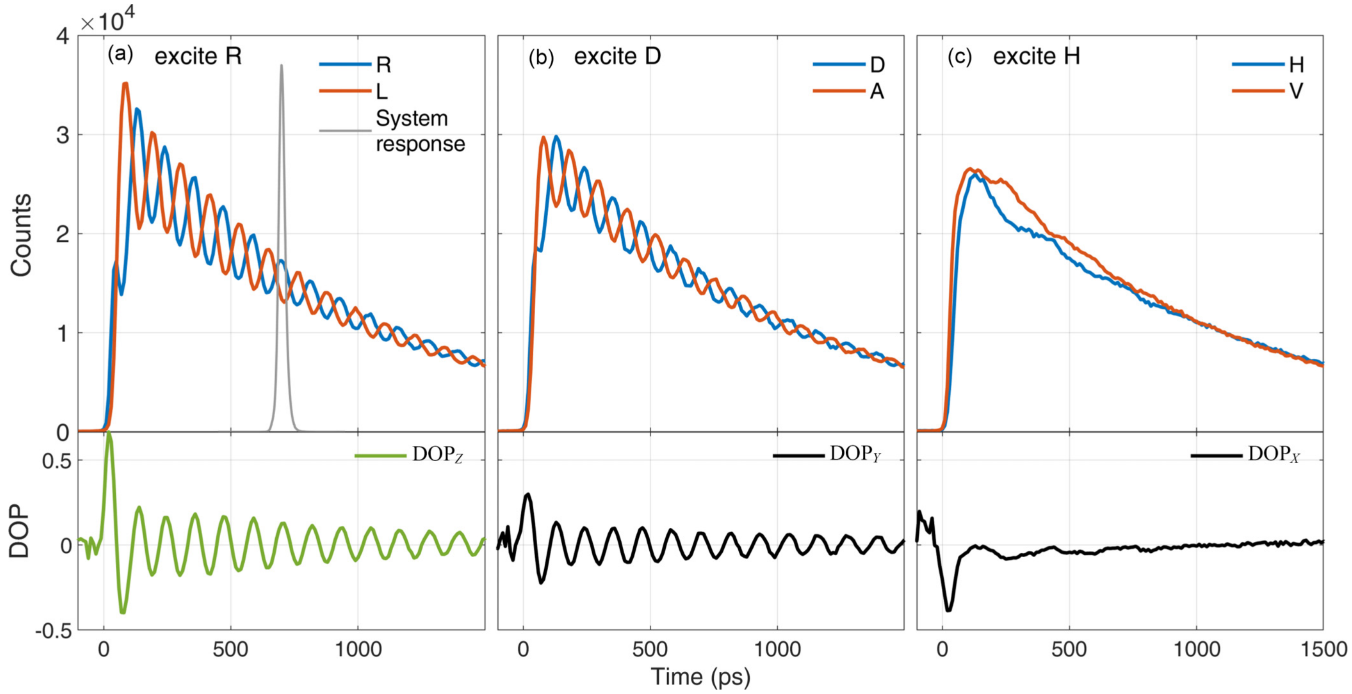

FIG. 3. Temporal evolution of the X^0 from the moment of its creation. (a)–(c) Top: Polarization-resolved evolution when the X^0 is excited with R-, D-, and H-polarized pulses and measured in the R/L, D/A, and H/V bases, respectively. Each time trace is normalized by the area beneath it. The system response is presented as a reference, where its amplitude is scaled to match the signal. Bottom: The degree of polarization (DOP) per basis, defined as $(P - \bar{P})/(P + \bar{P})$, where P and $\bar{P}$ are orthogonal polarizations. The circular DOP of (a) is plotted in green to match another use of the data later in Fig. 4.

In the H/V basis, we observe only a mild residual undulation of the polarization. From theoretical considerations, one would expect to observe no oscillations in this basis at all. First, because we are exciting with H or V, we assume to initialize the X^0 in one of its eigenstates, which stays constant in time [Eq. (4)]; second, even for an evolving state, its projection on the eigenstate basis (H/V) should stay constant [also Eq. (4)]. (Geometrically, a rotation around any axis in the Bloch sphere induces a constant projection on it.)

We suggest the following explanations for the residual undulations: For the latter point, we assume that the polarization projection alignment of our setup does not perfectly agree with the X^0 orientation. For the former point, we speculate that we fail to initialize the X^0 exclusively in one of its eigenstates because we inevitably excite a small portion of the orthogonal state. This is caused by the diagonal shape of the quasiresonance discussed earlier [Fig. 2(c)]: it forces any given excitation wavelength to couple both to the H and V resonance components, blocking the possibility of isolating only one of them. This renders the polarization of excitation as the only remaining degree of freedom to exclusively select one of the excited-state eigenstates. A contrary scenario can be found in Ref. [27], performed on QDs emitting at the 900 nm range. There, the quasiresonance profiles are flat and hence both polarization and wavelength are useful knobs for selective excitation.

We make an additional remark regarding the *visibility* of the oscillations in Fig. 3. The visibility is defined as the maximal value of the DOP during the oscillations. In the R/L basis, for example, it is bounded by 0.2, far from the ideal case of 1. We attribute this reduction, at least partially, to the response time uncertainty of our measurement setup (time jitter), which is around 28 ps. Since this value is on the same timescale as the X^0 oscillations, the convolution of the system's response with the measured signal reduces its visibility (see detailed analysis in Ref. [32]).

To further analyze the one-to-one correspondence between the excitation polarization and the generated X^0 spin state, also known as qubit writing, we use the same data set of 36 polarizations but focus only on those where the detection is in the circular basis, R/L. In Fig. 4, we show the circular DOP of the X^0 decay upon excitation with the six polarizations, R, L, D, A, H, and V, corresponding to the DOP_Z calculated in Eq. (7). To qualitatively analyze the qubit writing, we compare the phases of the DOP_Z signal with different excitation polarizations. We expect a DOP_Z signal with a $\pi/2$ phase shift for initializing in $|\pm Z\rangle$ and a $\pi/4$ phase shift compared to this when initializing in $|\pm Y\rangle$. Initialization in $|\pm X\rangle$ should not show any oscillations; see Eq. (8). Exciting with R (L) should initialize $|+Z\rangle$ ($|-Z\rangle$), while excitation with D (A) should initialize $|+Y\rangle$ ($|-Y\rangle$). Four vertical dashed lines between Figs. 4(a) and 4(b) mark four adjacent peaks of the four oscillations when excited with R, L, D, A. The color of each line matches the corresponding polarization. One can see that the phase spacing between the four polarizations is roughly $\pi/4$, as expected.

A quantitative measure of the four phases of R, D, L, and A reveals a deviation from a perfect $\pi/4$ spacing (see the Supplemental Material, Fig. 4 [31]). In addition, the H and V time traces reveal residual oscillation where a flat dependence is

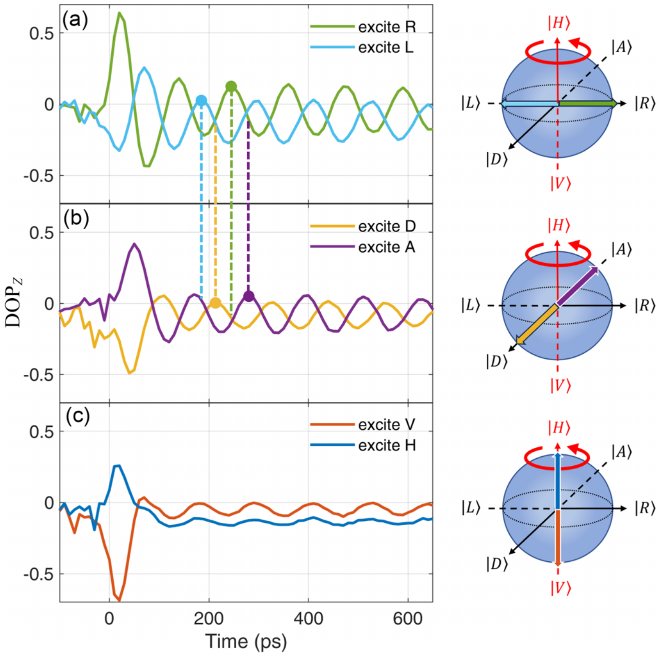

FIG. 4. Qubit writing. (a)–(c) Circular DOPs (DOP$_Z$) of the X^0 emission which follows an excitation with R/L, D/A, and H/V polarized pulses. Next to every panel, a color arrow marks the X^0 ideal state initialization in a Bloch sphere. The dashed colored vertical lines connecting (a) and (b) mark the four phases as determined by the maxima point of adjacent oscillation peaks.

expected, similar to the imperfection in Fig. 3(c). A probable reason for these imperfections is the challenge of ensuring that the six laser polarizations maintain orthogonality by the time they are absorbed in the QD. While prepared orthogonal in the laboratory frame, they can undergo skewing after passing several optical elements before reaching the QD.

Despite these imperfections, our results provide a proof of concept that the X^0 spin state can be arbitrarily prepared anywhere on the Bloch sphere. For a practical application, one can fine tune each of the excitation polarizations to perfectly match the targeted states. While compromising on polarization orthogonality in the laboratory frame, such fine tuning would still fulfill its task. As can be seen in the Supplemental Material, Fig. 3 [31], the polarization can be fine tuned to minimize oscillations in V in the expense of H, opposite to the case presented in Fig. 4(c). Thus, when combining those two excitation optimizations, one would be able to write either H or V.

B. X^- Larmor precession in a lifetime measurement

In the following section, we concentrate on a different spectral line—the negative trion, X^-, which we found in a different QD, i.e., QD2. Figure 5(a) presents the spectrum of QD2 and PLE of the X^-. In contrast to QD1, here we show the PL directly under quasiresonant and not under the above-band-gap excitation. Under these conditions, the X^- appears in the spectrum as a single line, emitting around 1541.6 nm. Similarly to the X^0, the PLE scan of the X^- reveals a diagonal shape of its quasiresonance, but with a slope of 0.82 ± 0.06. Our identification of the spectral line as an X^- is based mostly on its time-traced behavior presented in the next section. As a first hint, however, we observe no evidence of FSS. Observing FSS would immediately rule out a trion state (see Kramers' theorem, e.g., in Ref. [33]). Second, since a bare quasiresonant laser pumps electron-hole pairs into specific energy levels, we assume that it can maintain a steady-state population of only an exciton or a trion [30]. Power series performed with the quasiresonant laser bring us to the same conclusion (see the Supplemental Material, Fig. 1(b) [31]). We will return to the X^- identification by the end of the text, where we thoroughly discuss how we determined its sign.

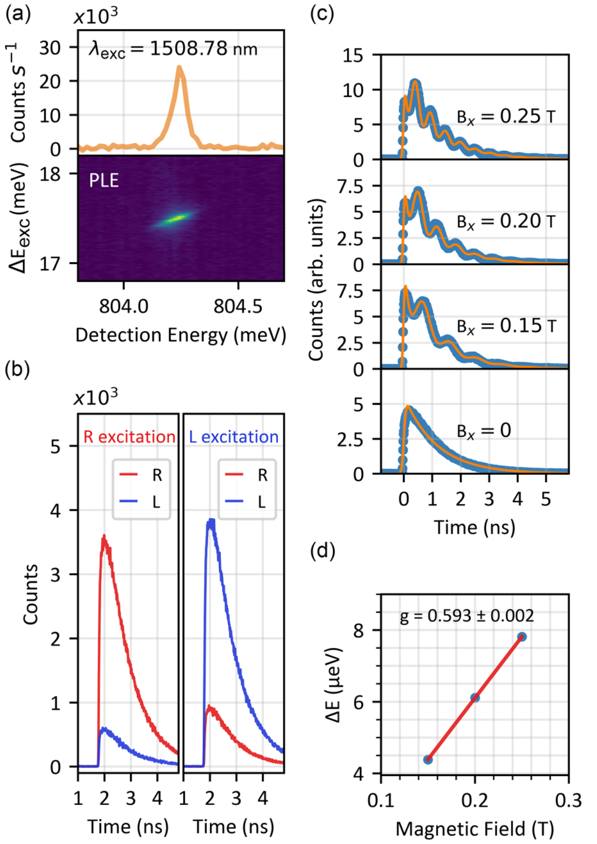

FIG. 5. X^- under quasiresonant excitation. (a) Spectral signature of the X^- and its PLE excitation. (b) Polarization memory. The X^- transition is excited once in R and once in L, while detected in the co- and cross polarizations. The integrated DOP$_Z$, also referred to as polarization memory, is measured to be 0.66 ± 0.07. (c) Time trace of the X^- decay at different values of an in-plane magnetic field. The oscillation frequency increases with higher fields and is extracted by fitting the time traces. (d) Linear fit of the energy splitting resulting from (c) vs magnetic field. From the linear slope, a g-factor absolute value of 0.593 ± 0.002 is calculated.

For the X^-, direct qubit writing is not possible, as explained in Sec. I. However, it may have polarization memory that is useful in initializing a matter spin, at least along the selection rules direction, $\hat{z}$ [33]. We say that a given optical transition has polarization memory if exciting it with R-polarized light results in predominantly R-polarized emission (with the L component suppressed), and vice versa. Indeed, in Fig. 5(b), we show how exciting the X^- in QD2 using its quasiresonance produces this effect. It is quantified in a

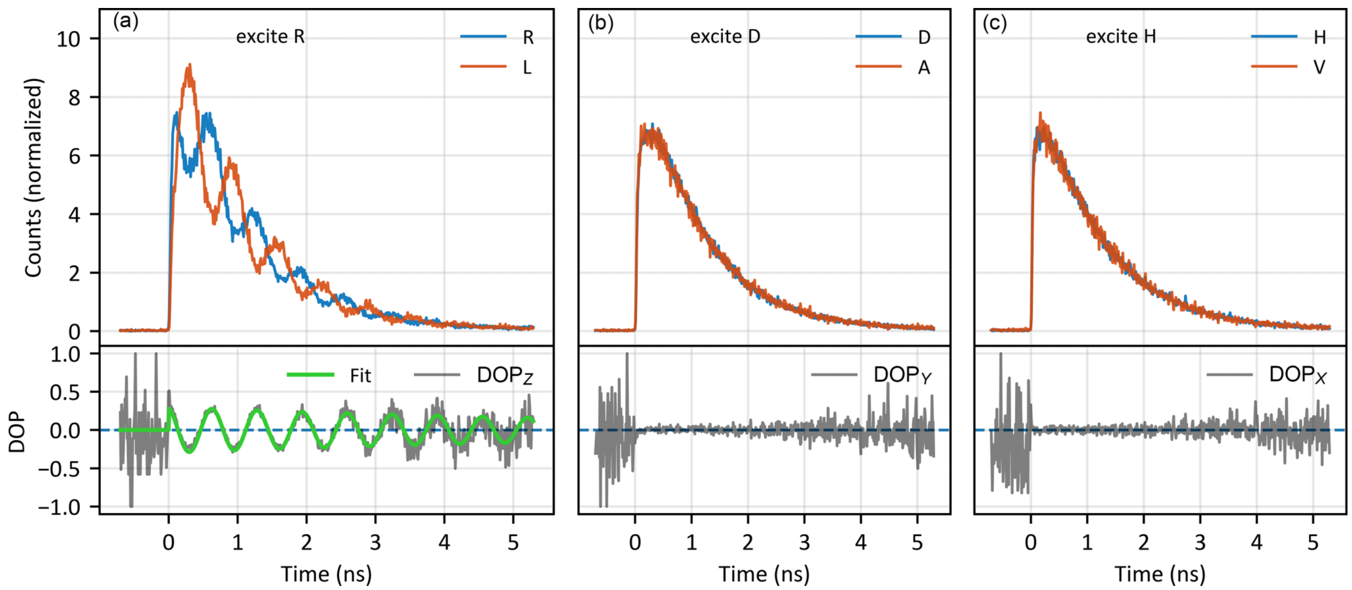

FIG. 6. Time trace of the X^- decay after pulsed excitation (same figure structure as Fig. 3 for the X^0). (a)–(c) Top: Excitation with R, D, and H polarizations while detection in the respective co- and cross polarizations. Bottom: DOP. As opposed to the X^0, oscillations are observed only in the R/L basis, not in D/A. Fitting the DOP$_Z$ yields a hole coherence time of 8.8 ± 2.3 ns.

similar way as the circular DOP, $\mathrm{DOP}_Z = (R - L)/(R + L)$, but time integrated over the entire signal. Using this definition, we find the polarization memory of the X^- to be 0.66 ± 0.07, where we averaged over excitation with R and L polarizations.

In Fig. 5(c), we show similar measurements, but where we add an external in-plane magnetic field. The oscillations observed in the DOP for different magnetic fields can be directly linked to the Larmor precession of the excited-level spin. For the X^-, it is determined by the unpaired hole. Fitting the oscillation frequency versus the magnetic field using a linear curve, we extract the in-plane hole g factor, $|g_h| = 0.593 \pm 0.002$ [Fig. 5(d)]. This value qualitatively agrees with previous works of Belykh *et al.* where they reported $|g_h| = 0.64 \pm 0.08$ [34,35].

To extract the spin coherence time of the excited state, i.e., the unpaired hole in the X^-, we resolve the oscillation polarization in its lifetime decay. A measurement under $B_x = 200$ mT is summarized in Fig. 6. This data set constitutes an analogous set to the one presented earlier for the X^0 in Fig. 3: it shows six time traces, divided into three polarization bases, R/L, D/A, and H/V. Each panel [Figs. 6(a)–6(c)] shows excitation in one polarization, and signal detection in the corresponding co- and cross polarizations. The full data set of 36 combinations of excitation and detection polarizations are presented in the Supplemental Material, Fig. 5 [31]. Note that the only conceptional difference between the X^0 and X^- cases is the mechanism lifting the spin degeneracy: while in the X^0 case, it is the FSS, here, it is the in-plane magnetic field.

Comparing Fig. 6 with the X^0 results in Fig. 3, we see a clear difference in the diagonal basis, D/A. While in the X^0 case, spin precession is clearly observed in this basis, for the X^-, it is not. This difference is a direct consequence of the X^- having a different final state after optical recombination than the X^0: while the X^0 decays into vacuum, the X^- decays into a two-level spin system formed by a single electron. Theoretically, this difference is evident comparing Eqs. (8) and (11).

Finally, we can use the X^- oscillation decay to extract the hole coherence time, T_2^*. We do that by fitting the DOP of the oscillations, presented in the lower panel of Fig. 6(a), with the function $e^{-t/T_2^*} \cos \omega t$. We find $T_2^* = 8.6 \pm 2.2$ ns. The relatively large error stems from the increasing statistical noise of the signal as it drops beyond the optical transition lifetime, $\tau = 1.135 \pm 0.022$ ns. Therefore, we suggest the lower margin of this value as a lower bound to the real coherence time, $T_2^* > 6.4$ ns, which is close to values recently obtained in the 900 nm range [36]. To the best of our knowledge, this bound is the highest reported so far for holes in telecom-emitting QDs.

C. X^- Larmor precession in a $g^2(\tau)$ correlation measurement

So far, we showed how a trion decay can reveal its *excited-level* spin precession. For the X^-, that was the hole. Here, we present a two-photon correlation measurement [$g^2(\tau)$] that allowed us to simultaneously observe both the excited-level *and the ground-level* spin precession. For that, we use a CW laser to quasiresonantly excite the optical transition, same as in the previous section. The laser polarization, as well as the two-photon projection polarizations, were all set to R. Similar measurements for InAs QDs emitting at the 900 nm range were recently reported in Refs. [36,37].

An example for this measurement, taken with an in-plane field of $B_x = 40$ mT, appears in Fig. 7(a). Note that the data displayed here are already normalized to a fit of the antibunching dip characteristic of a single-photon source. The full dataset including the fits appears in the Supplemental Material, Fig. 6 [31].

Due to fit imperfections, at $t = 0$, there is still a narrow remnant of the antibunching dip. In the dip vicinity, however, we observe signal undulations originating from spin dynamics. We analyze them by performing a Fourier

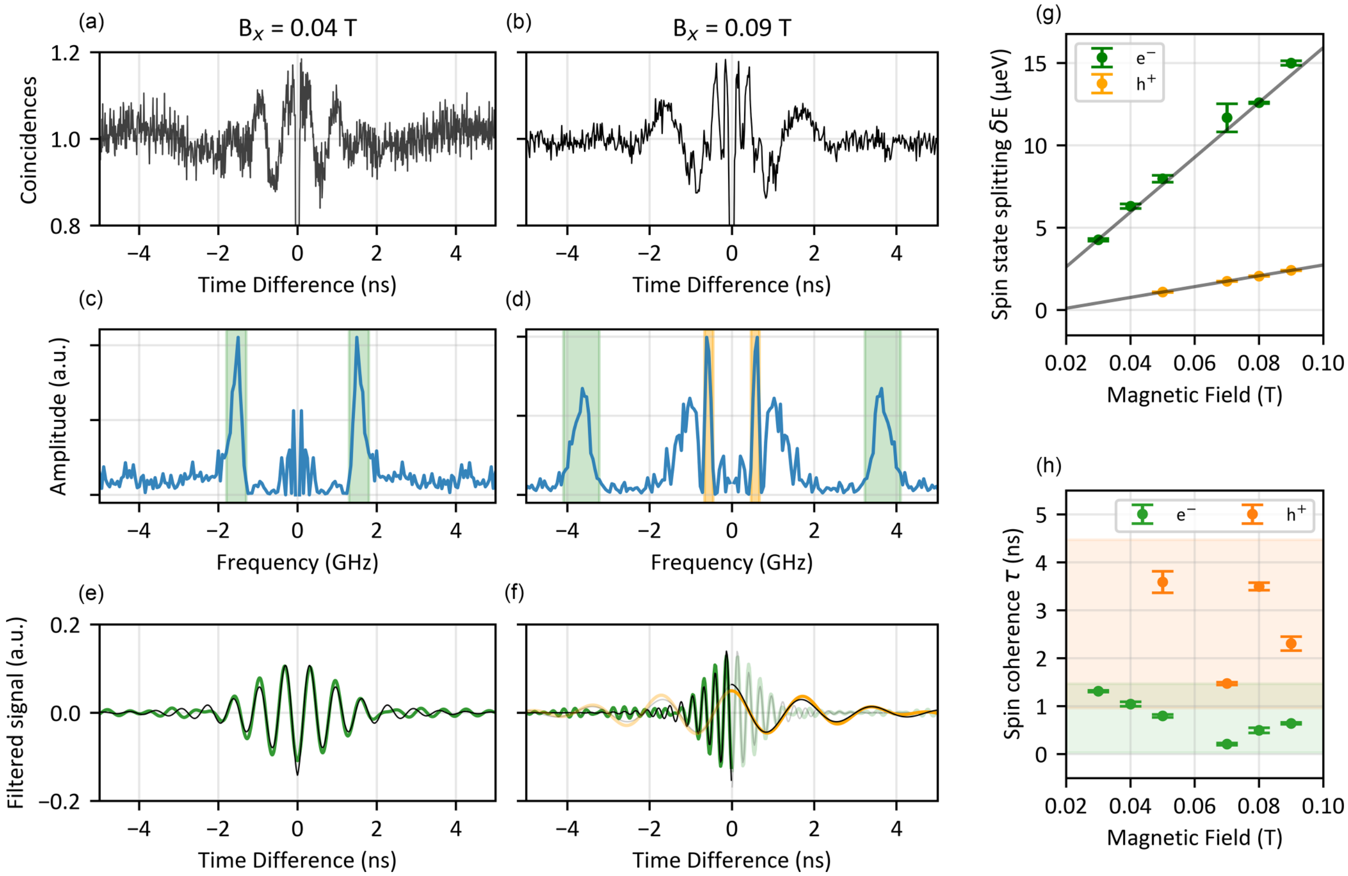

FIG. 7. Polarization-resolved $g^2(\tau)$ of the X^- under CW excitation. (a), (b) Two-photon coincidence histogram in the presence of in-plane magnetic fields with intensities 0.04 and 0.09 T, respectively. The data are normalized on a fit to the antibunching dip. (c), (d) Fourier transform of the signal showing its spectrum in the frequency domain. A dominant high frequency in the spectrum is identified as the ground-level electron Larmor precession and marked by a green background. A low-frequency component, emerging at 0.09 T, is attributed to the excited-level Larmor precession which is governed by the hole (orange background). (e), (f) Inverse transform of the isolated frequency regions of interest. Fitting a decaying exponential envelope, we extract the dephasing time of the oscillations, T_2^* (see text). (g) Electron and hole frequencies plotted against the applied magnetic field; linear fits reveal the corresponding absolute-value g factors, 2.876 ± 0.044 and 0.568 ± 0.004. The error bars are propagated from Gaussian fits to the selected frequency regions in (c) and (d) (see text). (h) Comparison of the oscillations decay times, interpreted as spin dephasing. Overall, the hole dephasing time is measured to be larger than the electron dephasing time, which is in line with the widespread premise.

transform on the signal, presented in Fig. 7(c). Aside from the low-frequencies concentration around 0, the Fourier spectrum reveals a clear component around $\pm 1.5\,\mathrm{GHz}$, marked in the figure by a green background. We then inverse transform the Fourier spectrum only with these frequencies, reconstructing a filtered $g^2(\tau)$ function that exhibits clear oscillations [Fig. 7(e)]. Fitting the data with the function $e^{-|t|/T_2^*}\cos(\omega|t|+\varphi)$, we extract the oscillation frequency ω and its coherence time T_2^*. Here, in contrast to the coherence time T_2^* in the excited state as measured above, the measured coherence time T_2^* is pump power dependent since it is extracted from a constantly driven system. The real coherence time, as observed in an undisturbed system, is expected to be higher; thus, all coherence times that are measured are lower bounds. To account for the errors, we fit the frequency concentrations in the Fourier spectrum with Gaussian peaks. These fits determine the exact frequency window we choose to inverse transform, and their errors are then propagated to ω and T_2^*.

We repeat this procedure for different magnetic fields between 30 and 90 mT. Figures 7(b), 7(d), and 7(f) display a similar measurement and analysis for $B_x = 90\,\mathrm{mT}$. Interestingly, the Fourier analysis in this case shows that a second prominent frequency component emerges [orange background in Fig. 7(d)]. The two components, converted to an energy splitting are summarized in Fig. 7(g) as a function of the magnetic field. A linear fit to each dataset allows us to extract the g factor of the oscillating spins. For the low frequency, we find $|g| = 0.568 \pm 0.004$ (orange data points). This value sufficiently agrees with the value $|g| = 0.593 \pm 0.002$ determined earlier from the lifetime oscillations [Fig. 5(c)]. Therefore, we attribute it to the excited-level spin. By the method of elimination, we conclude that the other frequency component is associated with the ground-level spin. In this case, the linear fit in Fig. 7(g) determines $|g| = 2.876 \pm 0.044$ (green data points).

Another interesting difference between the excited- and ground-level spin precessions lies in their measured coherence times. In Fig. 7(h), we plot them as a function of the applied magnetic field. A clear trend is observed: the coherence time of the excited-level spin is longer than that of the ground-level spin.

At this point, we can strengthen our identification of the studied trion as the negative one, X^-. It is based on the following two independent arguments:

(1) *g-factor comparison*. We associate the larger g factor, 2.876, to the electron. We do that following a fairly established theoretical argument: an electron in III-IV semiconductors has an s-shell unit-cell symmetry and, therefore, its g factor is expected to be isotropic. On the other hand, the hole has a p-shell symmetry, making its g factor anisotropic. Specifically, its in-plane g factor is expected to be smaller than the out-of-plane counterpart. Many studies have shown this phenomenon experimentally in InAs QDs emitting both at the 900 nm [38] and, lately, at the 1500 nm range [34].

(2) *Coherence time comparison*. The difference in the unit-cell symmetry between the two charge carriers also affects their interaction with the nuclei comprising the QD. The holes, having a p-symmetric unit-cell function, overlap less with these nuclei compared to the s-symmetric electrons. Consequently, a hole in a QD experiences a better effective isolation from the nuclei spin environment and has a longer coherence time. Studies on 900-nm-emitting QDs have reported a bound of 2.5 ns on the coherence time of the electron, and roughly 30 ns on the hole [29,39]. In this work, we measured the longer coherence time for the excited-level spin. The longest value, mentioned earlier in Sec. II B, was measured at 6.5 ns. Based on this comparison, we argue that the excited-level spin is governed by the hole.

Since both reasonings agree, we conclude that the ground-level spin is the electron and the excited-level spin is the X^-, governed by the hole.

III. SUMMARY

To conclude, we have studied the time-dependent selection rules of the X^0 and X^- optical transitions in a QD emitting in the telecom C-band. We have shown that we can conceptually write the state of the X^0 using a picosecond laser pulse tuned to its quasiresonance. We showed this by using the laser polarization to prepare the X^0 spin state in any arbitrary superposition. For the X^-, we measured its Larmor precession under an externally applied in-plane magnetic field. We did that once in a lifetime measurement and a second time in a polarization-sensitive $g^2(\tau)$ measurement. From these measurements, we extracted the electron and hole in-plane g factors, $|g_e| = 2.876 \pm 0.044$ and $|g_h| = 0.593 \pm 0.002$. In combination with the coherence times measured for both charge carriers, including $T_2^* > 6.4$ ns for the hole, we were able to unambiguously determine the sign of the studied trion as negative. These tools are useful for a future quest in identifying a positive trion—a promising candidate to act as a photon entangler for scalable quantum information schemes.

ACKNOWLEDGMENTS

The authors are grateful for financial support within the projects QR.X (Projects No. FKZ:16KISQ010 and No. FKZ:16KISQ013), QR.N (Projects No. FKZ:16KIS2207 and No. FKZ:16KIS2209), PhotonQ (Project No. FKZ:13N15759), and QECS (Project No. FKZ:13N16272) funded by the German Ministry for Research and Education (BMBF). We also acknowledge financial support by the State of Bavaria and the German research foundation (DFG) under Project No. INST 93/1007-1 LAGG.

M.J. and P.M. provided the sample. G.P., J.M.M., R.J., and M.H. built the spectroscopy setup, conducted the measurements, and carried out the data analysis. G.P. and J.M.M. wrote the paper with input from all authors. S.L.P, P.M, S.H., and T.H.-L. guided the work and acquired funding.

The authors declare no competing interests.

DATA AVAILABILITY

The data that support the findings of this article are not publicly available upon publication because it is not technically feasible and/or the cost of preparing, depositing, and hosting the data would be prohibitive within the terms of this research project. The data are available from the authors upon reasonable request.

APPENDIX A: SAMPLE

We study InAs/InGaAs QDs grown by metalorganic vapour-phase epitaxy (MOVPE) using the Stranski-Krastanov method on a GaAs substrate. Typically, lattice mismatch between InAs and GaAs causes strain on the QDs and limits their size such that the confined excitonic energy lies within the near-IR wavelength range. Pushing this material system to the telecom range requires finding ways to reduce this strain. In our sample, an InGaAs metamorphic (MMB) buffer layer was used before the wetting layer growth, allowing the QDs to form larger [40]. In previous studies, such QDs were estimated to be approximately 65 nm in diameter and 10 nm in height [41]. These studies also suggested that intermixing of gallium from the bulk reduces the indium content of these QDs to roughly 0.7 ($In_{0.7}Ga_{0.3}As$).

The sample embeds the QDs in a 1 λ planar cavity made from distributed Bragg reflectors, where the bottom mirror comprises 23 mirror pairs of AlAs/GaAs and the top mirror comprises 4 mirror pairs of TiO_2/SiO_2 which were sputter-deposited postgrowth. A sketch of the sample's layer structure can be found in the Supplemental Material [31].

APPENDIX B: EXPERIMENTAL SETUP

1. Excitation lasers

The following excitation lasers were used. Above band gap: 1064 nm diode laser. CW tunable laser for PLE scan: Toptica^{TD} CTL 1500. Pulsed laser for quasiresonant excitations: APE picoEmerald^{TD}. Precharacterization (not shown) was performed using a ps-pulsed Ti:sapphire Tsunami^{TD} laser from SpectraPhysics.

2. Setup polarization control

Polarization control was achieved using two pairs of liquid-crystal variable retarders (LCVRs). One pair was used for the excitation path and the other for the detection. These retarders allowed us to rotate the Poincaré sphere of polarization from the laboratory frame to the QD frame. In the QD frame, the H and V polarizations are defined along the FSS of the X^0. D and A are other orthogonal polarization pair in the sample plane, while the R and L are the circular polarization along the out-of-plane direction. For the measurements conducted on the X^-, polarization control in the detection was achieved using achromatic wave plates.

[1] P. Krantz, M. Kjaergaard, F. Yan, T. P. Orlando, S. Gustavsson, and W. D. Oliver, A quantum engineer's guide to superconducting qubits, Appl. Phys. Rev. **6**, 021318 (2019).

[2] C. Monroe, W. C. Campbell, L.-M. Duan, Z.-X. Gong, A. V. Gorshkov, P. W. Hess, R. Islam, K. Kim, N. M. Linke, G. Pagano, P. Richerme, C. Senko, and N. Y. Yao, Programmable quantum simulations of spin systems with trapped ions, Rev. Mod. Phys. **93**, 025001 (2021).

[3] F. Schäfer, T. Fukuhara, S. Sugawa, Y. Takasu, and Y. Takahashi, Tools for quantum simulation with ultracold atoms in optical lattices, Nat. Rev. Phys. **2**, 411 (2020).

[4] S. Slussarenko and G. J. Pryde, Photonic quantum information processing: A concise review, Appl. Phys. Rev. **6**, 041303 (2019).

[5] PsiQuantum team, A manufacturable platform for photonic quantum computing, Nature (London) **641**, 876 (2025).

[6] S. Bartolucci, P. Birchall, H. Bombín, H. Cable, C. Dawson, M. Gimeno-Segovia, E. Johnston, K. Kieling, N. Nickerson, M. Pant, F. Pastawski, T. Rudolph, and C. Sparrow, Fusion-based quantum computation, Nat. Commun. **14**, 912 (2023).

[7] C. Couteau, S. Barz, T. Durt, T. Gerrits, J. Huwer, R. Prevedel, J. Rarity, A. Shields, and G. Weihs, Applications of single photons to quantum communication and computing, Nat. Rev. Phys. **5**, 326 (2023).

[8] N. Akopian, N. H. Lindner, E. Poem, Y. Berlatzky, J. Avron, D. Gershoni, B. D. Gerardot, and P. M. Petroff, Entangled photon pairs from semiconductor quantum dots, Phys. Rev. Lett. **96**, 130501 (2006).

[9] H. Jayakumar, A. Predojević, T. Kauten, T. Huber, G. S. Solomon, and G. Weihs, Time-bin entangled photons from a quantum dot, Nat. Commun. **5**, 4251 (2014).

[10] N. H. Lindner and T. Rudolph, Proposal for pulsed on-demand sources of photonic cluster state strings, Phys. Rev. Lett. **103**, 113602 (2009).

[11] D. Buterakos, E. Barnes, and S. E. Economou, Deterministic generation of all-photonic quantum repeaters from solid-state emitters, Phys. Rev. X **7**, 041023 (2017).

[12] J. Borregaard, H. Pichler, T. Schröder, M. D. Lukin, P. Lodahl, and A. S. Sørensen, One-way quantum repeater based on near-deterministic photon-emitter interfaces, Phys. Rev. X **10**, 021071 (2020).

[13] P. Thomas, L. Ruscio, O. Morin, and G. Rempe, Fusion of deterministically generated photonic graph states, Nature (London) **629**, 567 (2024).

[14] I. Schwartz, D. Cogan, E. R. Schmidgall, Y. Don, L. Gantz, O. Kenneth, N. H. Lindner, and D. Gershoni, Deterministic generation of a cluster state of entangled photons, Science **354**, 434 (2016).

[15] D. Cogan, Z.-E. Su, O. Kenneth, and D. Gershoni, Deterministic generation of indistinguishable photons in a cluster state, Nat. Photon. **17**, 324 (2023).

[16] J.-P. Li, J. Qin, A. Chen, Z.-C. Duan, Y. Yu, Y. Huo, S. Höfling, C.-Y. Lu, K. Chen, and J.-W. Pan, Multiphoton graph states from a solid-state single-photon source, ACS Photon. **7**, 1603 (2020).

[17] D. Istrati, Y. Pilnyak, J. C. Loredo, C. Antón, N. Somaschi, P. Hilaire, H. Ollivier, M. Esmann, L. Cohen, L. Vidro, C. Millet, A. Lemaître, I. Sagnes, A. Harouri, L. Lanco, P. Senellart, and H. S. Eisenberg, Sequential generation of linear cluster states from a single photon emitter, Nat. Commun. **11**, 5501 (2020).

[18] N. Coste, D. A. Fioretto, N. Belabas, S. C. Wein, P. Hilaire, R. Frantzeskakis, M. Gundin, B. Goes, N. Somaschi, M. Morassi, A. Lemaître, I. Sagnes, A. Harouri, S. E. Economou, A. Auffeves, O. Krebs, L. Lanco, and P. Senellart, High-rate entanglement between a semiconductor spin and indistinguishable photons, Nat. Photon. **17**, 582 (2023).

[19] J. Wang, S. Paesani, Y. Ding, R. Santagati, P. Skrzypczyk, A. Salavrakos, J. Tura, R. Augusiak, L. Mančinska, D. Bacco, D. Bonneau, J. W. Silverstone, Q. Gong, A. Acín, K. Rottwitt, L. K. Oxenløwe, J. L. O'Brien, A. Laing, and M. G. Thompson, Multidimensional quantum entanglement with large-scale integrated optics, Science **360**, 285 (2018).

[20] P. Thomas, L. Ruscio, O. Morin, and G. Rempe, Efficient generation of entangled multiphoton graph states from a single atom, Nature (London) **608**, 677 (2022).

[21] R. Joos, S. Bauer, C. Rupp, S. Kolatschek, W. Fischer, C. Nawrath, P. Vijayan, R. Sittig, M. Jetter, S. L. Portalupi, and P. Michler, Coherently and incoherently pumped telecom C-band single-photon source with high brightness and indistinguishability, Nano Lett. **24**, 8626 (2024).

[22] J. Kim, J. Kaupp, Y. Reum, G. Peniakov, J. Michl, F. Kohr, M. Emmerling, M. Kamp, Y.-H. Cho, T. Huber-Loyola, S. Höfling, and A. T. Pfenning, Two-photon interference from an InAs quantum dot emitting in the telecom C-band, Adv. Quantum Technol., e2500069 (2025).

[23] Ł. Dusanowski, C. Nawrath, S. L. Portalupi, M. Jetter, T. Huber, S. Klembt, P. Michler, and S. Höfling, Optical charge injection and coherent control of a quantum-dot spin-qubit emitting at telecom wavelengths, Nat. Commun. **13**, 748 (2022).

[24] P. Laccotripes, T. Müller, R. M. Stevenson, J. Skiba-Szymanska, D. A. Ritchie, and A. J. Shields, Spin-photon entanglement with direct photon emission in the telecom C-band, Nat. Commun. **15**, 9740 (2024).

[25] F. Olbrich, J. Höschele, M. Müller, J. Kettler, S. Luca Portalupi, M. Paul, M. Jetter, and P. Michler, Polarization-entangled photons from an InGaAs-based quantum dot emitting in the telecom C-band, Appl. Phys. Lett. **111**, 133106 (2017).

[26] K. D. Zeuner, K. D. Jöns, L. Schweickert, C. R. Hedlund, C. N. Lobato, T. Lettner, K. Wang, S. Gyger, E. Schöll, S. Steinhauer, M. Hammar, and V. Zwiller, On-demand generation of entangled photon pairs in the telecom C-band with InAs quantum dots, ACS Photon. **8**, 2337 (2021).

[27] Y. Benny, S. Khatsevich, Y. Kodriano, E. Poem, R. Presman, D. Galushko, P. M. Petroff, and D. Gershoni, Coherent optical writing and reading of the exciton spin state in single quantum dots, Phys. Rev. Lett. **106**, 040504 (2011).

[28] I. Schwartz, E. R. Schmidgall, L. Gantz, D. Cogan, E. Bordo, Y. Don, M. Zielinski, and D. Gershoni, Deterministic writing and control of the dark exciton spin using single short optical pulses, Phys. Rev. X **5**, 011009 (2015).

[29] D. Cogan, O. Kenneth, N. H. Lindner, G. Peniakov, C. Hopfmann, D. Dalacu, P. J. Poole, P. Hawrylak, and D. Gershoni, Depolarization of electronic spin qubits confined in semiconductor quantum dots, Phys. Rev. X **8**, 041050 (2018).

[30] Y. Benny, Y. Kodriano, E. Poem, S. Khatsevitch, D. Gershoni, and P. M. Petroff, Two-photon photoluminescence excitation spectroscopy of single quantum dots, Phys. Rev. B **84**, 075473 (2011).

[31] See Supplemental Material at http://link.aps.org/supplemental/10.1103/3qh7-b696 for additional power series on the exciton and trion, extended datasets on the polarization calibrations, an extended dataset for the CW-autocorrelation measurement, as well as a sketch of the sample layer structure.

[32] R. Winik, D. Cogan, Y. Don, I. Schwartz, L. Gantz, E. R. Schmidgall, N. Livneh, R. Rapaport, E. Buks, and D. Gershoni, On-demand source of maximally entangled photon pairs using the biexciton-exciton radiative cascade, Phys. Rev. B **95**, 235435 (2017).

[33] E. Poem and D. Gershoni, Radiative cascades in semiconductor quantum dots, in *Handbook of Luminescent Semiconductor Materials*, edited by L. Bergman and J. L. McHale (CRC Press, Boca Raton, FL, 2011), pp. 321–364.

[34] V. V. Belykh, A. Greilich, D. R. Yakovlev, M. Yacob, J. P. Reithmaier, M. Benyoucef, and M. Bayer, Electron and hole g factors in InAs/InAlGaAs self-assembled quantum dots emitting at telecom wavelengths, Phys. Rev. B **92**, 165307 (2015).

[35] V. V. Belykh, D. R. Yakovlev, J. J. Schindler, E. A. Zhukov, M. A. Semina, M. Yacob, J. P. Reithmaier, M. Benyoucef, and M. Bayer, Large anisotropy of electron and hole g factors in infrared-emitting InAs/InAlGaAs self-assembled quantum dots, Phys. Rev. B **93**, 125302 (2016).

[36] Y. Serov, A. Galimov, D. S. Smirnov, M. Rakhlin, N. Leppenen, G. Klimko, S. Sorokin, I. Sedova, D. Berezina, Y. Salii, M. Kulagina, Y. Zadiranov, S. Troshkov, T. V. Shubina, and A. A. Toropov, Hidden anisotropy controls spin-photon entanglement in a charged quantum dot, Phys. Rev. Appl. **23**, 044019 (2025).

[37] N. Coste, M. Gundin, D. A. Fioretto, S. E. Thomas, C. Millet, E. Mehdi, N. Somaschi, M. Morassi, M. Pont, A. Lemaître, N. Belabas, O. Krebs, L. Lanco, and P. Senellart, Probing the dynamics and coherence of a semiconductor hole spin via acoustic phonon-assisted excitation, Quantum Sci. Technol. **8**, 025021 (2023).

[38] B. J. Witek, R. W. Heeres, U. Perinetti, E. P. A. M. Bakkers, L. P. Kouwenhoven, and V. Zwiller, Measurement of the g-factor tensor in a quantum dot and disentanglement of exciton spins, Phys. Rev. B **84**, 195305 (2011).

[39] A. Bechtold, D. Rauch, F. Li, T. Simmet, P.-L. Ardelt, A. Regler, K. Müller, N. A. Sinitsyn, and J. J. Finley, Three-stage decoherence dynamics of an electron spin qubit in an optically active quantum dot, Nat. Phys. **11**, 1005 (2015).

[40] R. Sittig, C. Nawrath, S. Kolatschek, S. Bauer, R. Schaber, J. Huang, P. Vijayan, P. Pruy, S. L. Portalupi, M. Jetter, and P. Michler, Thin-film InGaAs metamorphic buffer for telecom C-band InAs quantum dots and optical resonators on GaAs platform, Nanophotonics **11**, 1109 (2022).

[41] C. Carmesin, F. Olbrich, T. Mehrtens, M. Florian, S. Michael, S. Schreier, C. Nawrath, M. Paul, J. Höschele, B. Gerken, J. Kettler, S. L. Portalupi, M. Jetter, P. Michler, A. Rosenauer, and F. Jahnke, Structural and optical properties of InAs/(In)GaAs/GaAs quantum dots with single-photon emission in the telecom C-band up to 77 K, Phys. Rev. B **98**, 125407 (2018).